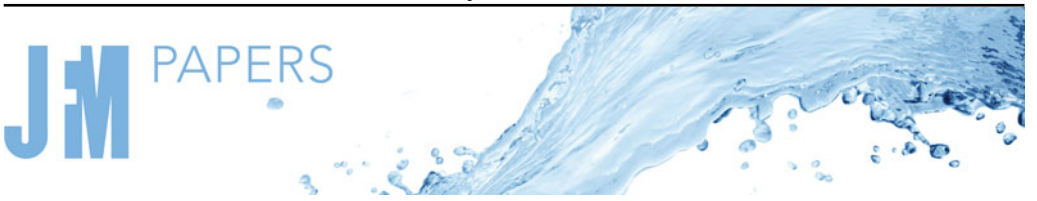
*J. Fluid Mech.* (2026), *vol.* 1034, A60, doi:10.1017/jfm.2026.11550




# Two-component inner–outer scaling model for the wall-pressure spectrum at high Reynolds number

**Jonathan M.O. Massey**[1], **Alexander J. Smits**[2] and **Beverley J. McKeon**[1]

[1]Center for Turbulence Research, Stanford University, Stanford, CA 94305, USA

[2]Department of Mechanical and Aerospace Engineering, Princeton University, Princeton, NJ 08544, USA

**Corresponding author:** Jonathan M.O. Massey, masseyj@stanford.edu

(Received 30 July 2025; revised 19 February 2026; accepted 10 April 2026)

Wall-pressure fluctuations beneath turbulent boundary layers (BLs) drive noise and structural fatigue through interactions between fluid and structural modes. Conventional predictive models for the spectrum – such as the widely accepted Goody model (2004 *AIAA J.*, vol. 42 (9), pp. 1788–1794) – fail to capture the energetic growth in the low-frequency range that occurs at high Reynolds number, while at the same time over-predicting the variance. To address these shortcomings, two semi-empirical models are proposed for the wall-pressure spectrum in canonical turbulent BLs, pipes and channels for friction Reynolds numbers $\delta^+$ ranging from 180 to 47 000. Consistent with the approach outlined modelling the streamwise Reynolds stress in the recent work of Gustenyov *et al.* (2025 *J. Fluid Mech.,* vol. 1016, A23), the models are based on consideration of two spectral components that represent the contributions to the wall-pressure fluctuations from inner-scale motions and outer-scale motions. The first model expresses the pre-multiplied spectrum as the sum of two overlapping log-normal components: an inner-scaled term that is $\delta^+$-invariant and an outer-scaled term whose amplitude broadens smoothly with $\delta^+$. Calibrated against large-eddy simulations, direct numerical simulations and recent high-$\delta^+$ pipe data, it reproduces the inner-scaled peak and the emergence of an outer-scaled peak at large $\delta^+$. The second model, developed around newly available pipe data, uses theoretical arguments to prescribe the spectral shapes of the inner and outer components. Embedding the $\delta^+$-dependence in smooth asymptotic functions yields a formulation that varies continuously with $\delta^+$ and generalises beyond the calibration range. Both models capture the full spectrum and recover the observed logarithmic growth of

© The Author(s), 2026. Published by Cambridge University Press. This is an Open Access article, distributed under the terms of the Creative Commons Attribution licence (https://creativecommons.org/licenses/by/4.0/), which permits unrestricted re-use, distribution and reproduction, provided the original article is properly cited.



https://doi.org/10.1017/jfm.2026.11550 Published online by Cambridge University Press

its variance, providing a compact, physics-informed empirical representation for more accurate engineering predictions of wall-pressure fluctuations.

**Key words:** turbulent boundary layers, turbulence modelling

## 1. Introduction

Predicting radiated noise and mitigating structural resonance in aircraft and marine structures depend critically on accurate models of wall-pressure behaviour in turbulent wall-bounded flows. A complete description of the fluctuating wall-pressure field is given by the three-dimensional wavenumber–frequency spectrum, $\phi_{pp}(f, k_x, k_z)$ (Zhao *et al.* 2025), where $f$ is the frequency and $k$ is the wavenumber. In canonical incompressible wall-bounded flows – e.g. zero-pressure-gradient boundary layers (BLs) and smooth-wall internal flows – this spectrum exhibits a convective ridge and a low-frequency range. The convective ridge maps closely to Taylor's frozen turbulence hypothesis (Taylor 1938), but shows weak scale dependence (Del Álamo & Jiménez 2009), with a noticeable reduction from the typical inner-normalised mean convection velocity $U_c^+ \equiv U_c/u_\tau \approx 10$ at high wavenumbers, where $u_\tau$ is the friction velocity.

In most experiments, however, only the one-dimensional frequency spectrum $\phi_{pp}(f)$ is available. Because $\phi_{pp}(f)$ is obtained by integrating over wavenumbers (and implicitly over a range of scale-dependent convection velocities), features in $\phi_{pp}(f)$ cannot be uniquely attributed to specific regions of $k$–$\omega$ space, where $\omega$ is the radial frequency. In this paper we therefore focus on the scaling behaviour and evolution of the one-dimensional (1-D) spectral features.

This restriction – although full-aperture experimental arrays are becoming more ubiquitous (e.g. Damani *et al.* 2025)) – has motivated a family of semi-empirical models that reconstruct $\phi_{pp}(f, k_x, k_z)$ from $\phi_{pp}(f)$ (Corcos 1964; Smol'Yakov 2006; Hwang, Bonness & Hambric 2009). Consequently, the fidelity of $\phi_{pp}(f)$ as a function of the friction Reynolds number, $\delta^+$, directly governs the accuracy of predicted wall-pressure behaviour and underpins efforts to scale its variance (Farabee & Casarella 1991; Hu, Morfey & Sandham 2006; Klewicki, Priyadarshana & Metzger 2008; Schlatter & Örlü 2010; Lee & Moser 2015; Panton, Lee & Moser 2017; Hasan *et al.* 2025).

A widely used model for the wall-pressure spectrum in zero-pressure-gradient BLs is that proposed by Goody (2004). Other models are available, but are limited by their use of low-mid $\delta^+$ datasets; see Damani *et al.* (2025) for a recent comparison of available models. The Goody model is derived from $\{Re_{\theta_i}\}_{i=1}^{7} \subset [1.4 \times 10^3, 2.34 \times 10^4] \mapsto \{\delta_i^+\}_{i=1}^{7} \subset [650, 7\,650]$. It encapsulates distinct inner and outer time scales and echoes Bradshaw's early recognition of inner- and outer-scaled contributions (Bradshaw 1967). Its key assumption is an overlap region in which dimensional analysis predicts an $f^{-1}$ scaling. Recent high-$\delta^+$ measurements reveal, however, an outer-scaled spectral peak that violates this simple $f^{-1}$ behaviour and leads to errors in the Goody model at high Reynolds number (Klewicki *et al.* 2008; Fritsch *et al.* 2020, 2022; Gibeau & Ghaemi 2021; Damani *et al.* 2024*a*, 2025; Dacome *et al.* 2025).

To develop models that correctly capture both the high-Reynolds-number behaviour of the spectrum, and the Reynolds-number dependence of the variance, we use data from boundary-layer, pipe and channel flows over a very wide range of Reynolds numbers $\{\delta_i^+\}_{i=1}^{19} \subset [180, 4.7 \times 10^4]$ (figure 1). In particular, we exploit the diagnostic power of the pre-multiplied spectrum, $f\phi_{pp}$, which more clearly separates inner- and



https://doi.org/10.1017/jfm.2026.11550 Published online by Cambridge University Press

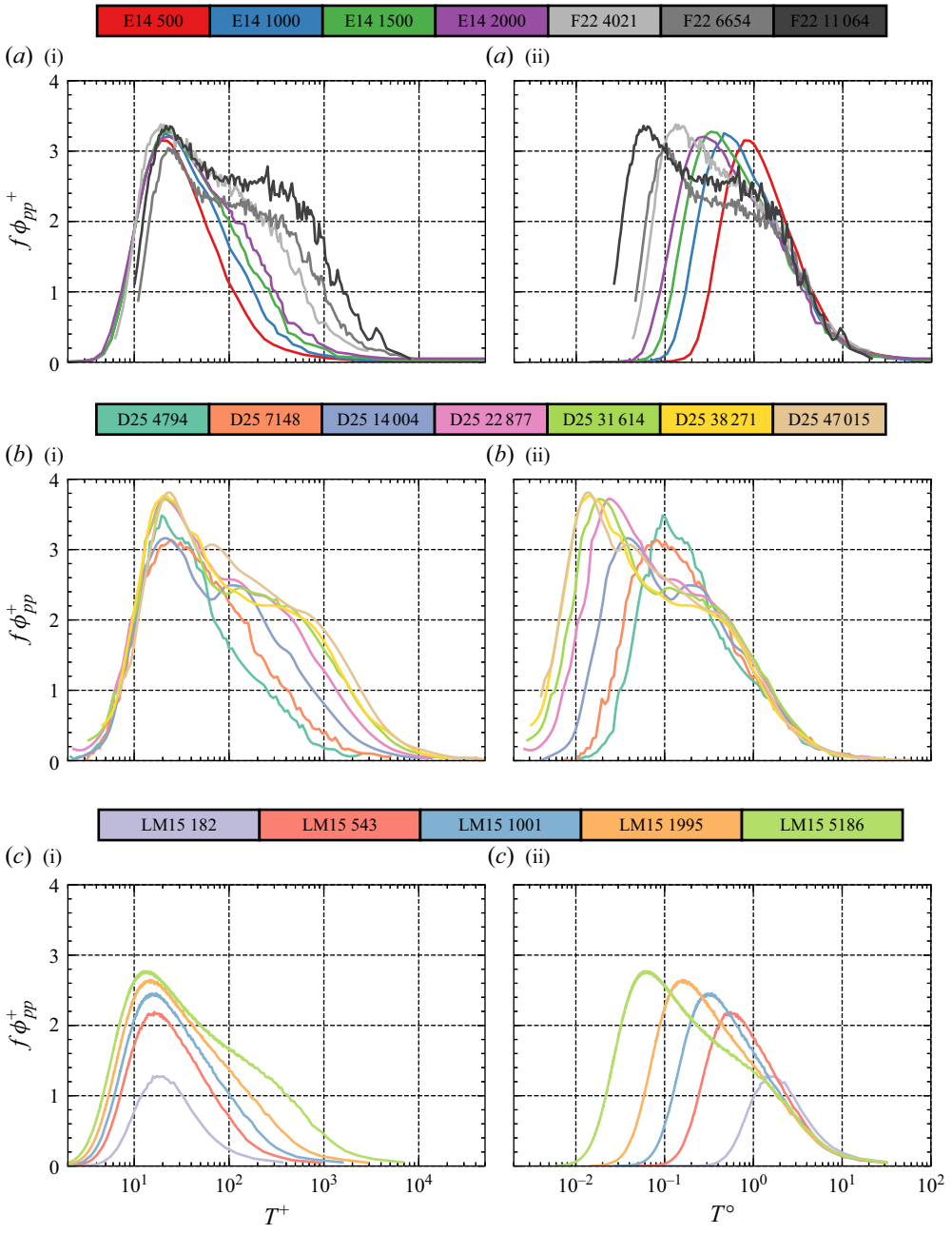



Figure 1. Pre-multiplied spectra of wall-pressure fluctuations. (*a*i,*b*i,*c*i): inner scaling. (*a*ii,*b*ii,*c*ii): outer scaling. (*a*) BLs. Highly resolved LES data from Eitel-Amor *et al.* (2014) for $\delta^{+} = 500$ to 2000, experimental data from Fritsch *et al.* (2020, 2022) for $\delta^{+} = 4021$ to 11 064. (*b*): Pipes. Experiments by Dacome *et al.* (2025) for $\delta^{+} = 4794$ to 47 015. (*c*): Channels. Direct numerical simulation (DNS) data from Lee & Moser (2015) for $\delta^{+} = 180$ to 5200.

outer-scale contributions than the conventional log–log representation. The inner-scaled spectrum is $\phi_{pp}^{+} = \phi_{pp}/\tau_w^2$ where $\tau$ is the wall shear stress, so the pre-multiplied form is $f\phi_{pp}{}^{+}$ and the variance is $\langle p_w^2\rangle^{+} = \int_0^{\infty} f\phi_{pp}{}^{+}\,\mathrm{d}\log f$. Superscript $(\cdot)^{+}$ denotes



https://doi.org/10.1017/jfm.2026.11550 Published online by Cambridge University Press

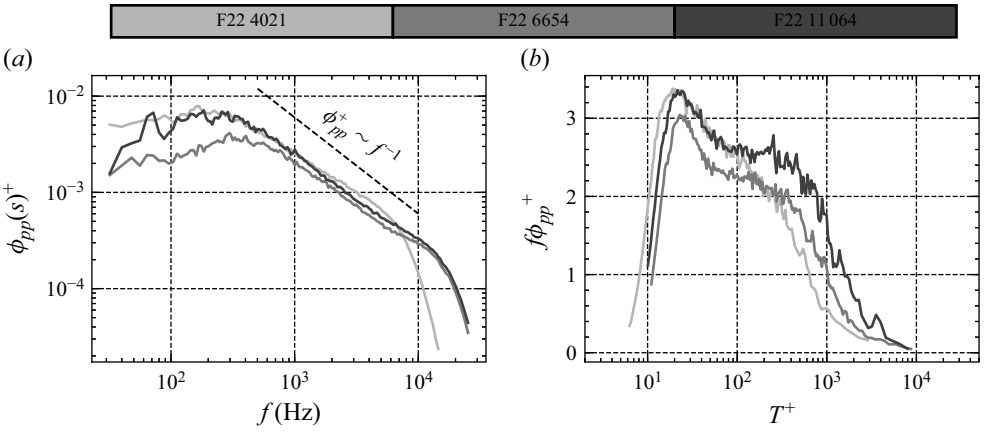



Figure 2. Spectra of wall-pressure fluctuations in BLs. Smooth-wall data at $\delta^+ = 4\,021$ to 11 064 (Fritsch *et al.* 2020, 2022, grey lines). (*a*) Log–log form. (*b*) Pre-multiplied form.

normalisation by the viscous length $\nu/u_\tau$, where $\nu$ is the kinematic viscosity, while superscript $(\cdot)^o$ denotes normalisation by $\delta$, the 99 % boundary-layer thickness or pipe/channel half-height and $U_e$, the free-stream or centreline velocity. Frequency and period are related by $f = 1/T$, while $T^+ = Tu_\tau^2/\nu$ and $T^o = TU_e/\delta$ are the inner- and outer-scaled periods, respectively. The boundary-layer data are taken from highly resolved large-eddy simulations (LES) (Eitel-Amor, Örlü & Schlatter 2014) and experiments (Fritsch *et al.* 2020, 2022); the pipe-flow data are from the CICLoPE facility (Dacome *et al.* 2025); and the channel-flow data are from DNS (Lee & Moser 2015). Further details on the data are given in Appendix A.

We see that the pre-multiplied spectra all share similar features. First, the data collapse at low values of $T^+$ (high frequencies) in inner scaling, consistent with the findings of Pirozzoli & Wei (2025), who note the universality at the small-scale end of the spectra. In outer scaling at high values of $T^o$ (low frequencies), the spectra also collapse. Second, there is a peak located at $T^+ \approx 10{-}15$ for channels and $T^+ \approx 20$ for BLs and pipes. This peak is identified with the start of the inner-scaled peak and its magnitude varies with Reynolds number at low Reynolds numbers, more so for the internal flows than for the BL. Third, as the Reynolds number increases, there is increased energy content at low frequencies ($T^o = O(1)$), marking the development of the low-frequency portion.

In what follows, we use these observations to develop two semi-empirical models for the wall-pressure spectrum that explicitly represent the bimodal picture as a sum of inner- and outer-scaled spectral components. The models apply to boundary-layer, pipe and channel flows, and capture the pre-multiplied spectra at high Reynolds number while reproducing the Reynolds-number-dependent behaviour of the variance in agreement with previous work.

## 2. Modelling approach

In the Goody model, the $\delta^+$-dependence is captured through the time-scale ratio between the inner and outer scales, which presents as the growth of the $f^{-1}$ region in $\phi_{pp}$ illustrated in figure 2. Figure 3 shows the pre-multiplied spectra for the boundary-layer data and the prediction from the Goody model. The model displays a strong Reynolds-number dependence that, although very far off at the peak, captures the frequency-dependent growth and decay of the inner and outer scales faithfully. A weakness of the Goody



https://doi.org/10.1017/jfm.2026.11550 Published online by Cambridge University Press

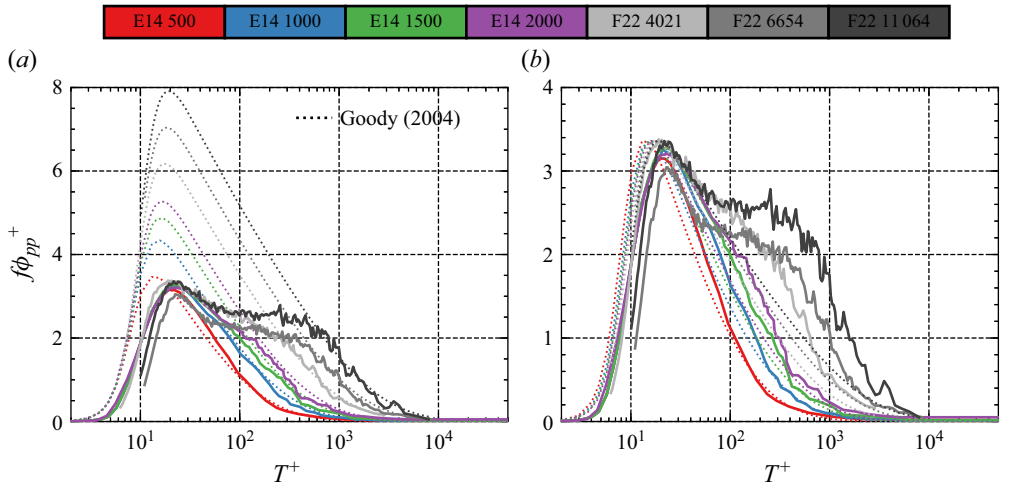



Figure 3. Pre-multiplied spectra of wall-pressure fluctuations in BLs compared with Goody's (2004) model. (*a*) Model as given. (*b*) Model normalised so that the peak value is fixed at 3.36. Highly resolved LES data from Eitel-Amor *et al.* (2014) for $\delta^+ = 500$ to 2000, experimental data from Fritsch *et al.* (2020, 2022) for $\delta^+ = 4021$ to 11 064. Model predictions are shown by the dashed lines colour coded to the data.

model is that the matching between the inner and outer time scales is done via a single modified Lorentzian distribution. A symptom of the fixed shape is that the peak separating the inner- and outer-scale behaviour in the pre-multiplied form has to rise to stay faithful to the gradients of growth and decay of these contributions. The result is a gross mismatch with the data at high Reynolds number (figure 3), although both the inner and outer growth and decay are captured faithfully. Even after normalising the inner peak to remove Reynolds-number dependence, Goody's model fails to capture the growth in low-frequency (high-$T^+$) energy – the low-frequency portion of the 1-D spectrum.

The models advanced here build on literature focusing on the increasing energy and length scales of the turbulent structures (Smits, McKeon & Marusic 2011) as well as their invariance when scaled with inner and outer variables (Wei *et al.* 2005). To solve for the pressure, we would need access to the full, 3-D velocity field. Instead, we use measurements of the wall pressure with the knowledge that the wall pressure is related to the velocity field through the pressure-Poisson equation, but this connection is non-local and involves multiple source terms; we therefore invoke it only as qualitative motivation. The wall-pressure spectrum $\phi_{pp}$ is constructed in the frequency domain by combining two spectral components that broadly represent the contributions to the wall-pressure fluctuations from inner-scaled motions ($g_1$) and outer-scaled motions ($g_2$).

At sufficiently large $\delta^+$, we expect the contributions represented by $g_1$ to approach an asymptotically inner-scaled form. This expectation is consistent with the observed tendency toward universality at the small-scale end of wall-pressure spectra and with data-driven decompositions of near-wall velocity spectra indicating that, once sufficient scale separation is achieved, the inner contribution collapses in inner scaling (e.g. Baars & Marusic 2020). These arguments are heuristic: the mapping from velocity statistics to wall-pressure fluctuations is indirect and non-local, so we treat the saturation of $g_1$ as an empirically guided modelling constraint. Experimental uncertainty and competing influences from several well-established processes make it difficult to specify the precise $\delta^+$ at which this invariance is achieved. Nevertheless, established scaling arguments for the velocity field and its decomposition into inner, intermediate and outer contributions



https://doi.org/10.1017/jfm.2026.11550 Published online by Cambridge University Press

provide a useful qualitative guide (Smits *et al.* 2011). Consistent with this, data-driven decompositions show that once a minimal scale separation is present, the near-wall contribution associated with $g_1$ collapses in inner scaling and becomes effectively $\delta^+$-invariant. The second component $g_2$ is expressed in outer time $T^o$ (outer scaled in this kinematic sense), with its Reynolds-number dependence representing the growing contribution and bandwidth of intermediate/large scales when projected onto $\phi_{pp}(f)$.

These contributions are modelled as spectral distributions in ${f\phi_{pp}}^+$ that overlap in the $T$ domain. The energy is taken to be a linear summation over the two spectral components. That is,

$$ {f\phi_{pp}}^+ = g_1(T^+;\,\delta^+) + g_2(T^o;\,\delta^+). \tag{2.1} $$

Since ${f\phi_{pp}}^+ = g_1(T^+;\,\delta^+) + g_2(T^o;\,\delta^+)$ is evaluated at a fixed physical frequency $f = 1/T$, the inner- and outer-normalised periods are linked by $T^o = T^+\,(U_e^+/\delta^+)$ with $U_e^+ \equiv U_e/u_\tau$ (here, $U_e$ denotes the appropriate outer velocity scale). Hence, both components are summed at the same $f$ without invoking a convection velocity; $U_c$ enters only when mapping to $k_x = 2\pi f/U_c$. In the present comparisons, $U_e^+$ is taken directly from the underlying datasets and therefore no additional empirical model is required to relate $T^+$ and $T^o$. For extrapolation to higher $\delta^+$, standard friction-law/log-law correlations may be used to estimate the slow variation of $U_e^+$ with Reynolds number. At low-$\delta^+$, the inner and outer scales overlap significantly, confusing the distinction between the two components. As $\delta^+$ increases, the two components separate in frequency space, with $g_1$ dominating at high frequencies (low $T^+$) and $g_2$ dominating at low frequencies (high $T^o$). The models proposed below aim to capture this transition from inner to outer scaling as $\delta^+$ increases.

An immediate consequence of (2.1) is that we expect to see the appearance of an overlap region at a sufficiently high Reynolds number where $f\phi_{pp}$ is neither a function of $T^+$ nor $T^o$, that is, where $g_1 + g_2 = constant$, so that there is an $f^{-1}$ region in $\phi_{pp}$ and a plateau region in $f\phi_{pp}$ (figure 2). (It is this plateau region that the Goody model fails to capture.) In wavenumber space, this corresponds to a $k^{-1}$ region, where $k = 2\pi f/U_c$ is the streamwise wavenumber and $U_c$ is the convection velocity in this wavenumber range. This result is in accordance with numerous previous studies (see, for example, Klewicki *et al.* 2008), and we see this overlap region develop with increasing Reynolds number in figure 2, in both the log–log and pre-multiplied representations. Klewicki *et al.* also cited Panton & Linebarger (1974) in observing that, if $U_c$ is not constant, the slope of the $k^{-1}$ region in the wavenumber spectrum is preserved as an $f^{-1}$ region in the corresponding frequency spectrum.

We offer two versions of this general model. The first version (model A) acts as a low-parameter estimation representing the inner and outer components by two log-normal distributions in the pre-multiplied spectrum. Model A follows the approach taken by Gustenyov, Bailey & Smits (2025) in representing the spectrum of the streamwise Reynolds stress, providing a family of models for the velocity and pressure spectra. In the second version, we aim to incorporate the known behaviour of the pressure spectra using a modified Lorentzian spectral shape, similar to the approach taken by Goody (2004), but with the important separation of the contribution from inner-and outer-scaled spectral components. This approach allows the model to incorporate known asymptotic limits on the spectrum, which may therefore allow a more confident extrapolation to very high Reynolds numbers, such as those encountered in realistic engineering examples. The behaviour of both models is guided by the theoretical understanding of the wall-pressure spectrum and by empirical observations of its scaling with Reynolds number, with the aim



https://doi.org/10.1017/jfm.2026.11550 Published online by Cambridge University Press

| | $A_1$ | $\sigma_1$ | $\overline{T}^+$ | $A_2$ | $\sigma_2$ | $\overline{T}^o$ | $r_1$ | $r_2$ |
|---|---|---|---|---|---|---|---|---|
| BL | 2.20 | 3.90 | 20 | $1.40(\log\delta^+ - 2.2)$ | 8.18 | 0.82 | 0.50 | 7 |
| Pipe | $2.90(1 - 1000/\delta^+)$ | 4.30 | 20 | $0.91(\log\delta^+ - 2.2)$ | 10.0 | 0.18 | 0.50 | 7 |
| Channel | $2.10(1 - 100/\delta^+)$ | 4.40 | 12 | $0.90(\log\delta^+ - 2.2)$ | 10.0 | 0.60 | 0.50 | 3 |

Table 1. Model A best-fit constants.

of providing a continuous model that captures the transition from inner to outer scaling as $\delta^+$ increases.

## 3. Model definitions

### 3.1. *Model A – log normal*

For $g_1$ and $g_2$ in model A, we will assume that their contributions to the pre-multiplied energy distribution can be modelled using log-normal distributions in $T$. That is, we propose

$$g_1 = A_1 r_v \exp\left[-\left(\frac{\log T^+ - \log \overline{T}^+}{\log \sigma_1}\right)^2\right], \tag{3.1}$$

$$g_2 = A_2 r_v \exp\left[-\left(\frac{\log T^o - \log \overline{T}^o}{\log \sigma_2}\right)^2\right]. \tag{3.2}$$

The energy content is thus distributed around the (non-dimensional) periods for the inner and outer contributions to the spectrum ($\overline{T}^+$, $\overline{T}^o$), with the frequency range of the distributions described by ($\sigma_1$, $\sigma_2$). Here, $\overline{T}^+$ represents the temporal centre of the energetic contributions from the inner component, while $\overline{T}^o$ represents the centre of the contributions from the outer component and $\sigma_1$, $\sigma_2$ represent the width of the distributions, controlling their frequency range. A viscous damping term $r_v$ is active for $T^+ \lesssim 15$, defined by the smooth step function

$$r_v = \frac{\exp(r_1 T^+)}{\exp(r_1 r_2) + \exp(r_1 T^+)}; \tag{3.3}$$

$r_v$ captures the development of the inner component' contribution towards its saturation at high $\delta^+$; this development will vary between BLs and internal flows. Importantly, the invariance of $g_1$ at high $\delta^+$ – for pipe and channel flow – is enforced by the asymptote of $r_v$ to 1 at sufficient $\delta^+$.

The best fit constants for model A are provided in table 1. The most notable differences among the three flow types are in the Reynolds-number dependence of $A_1$ (which becomes negligible at high Reynolds number) and the location of the peaks as given by $\overline{T^+}$ and $\overline{T^o}$.

### 3.2. *Model B – modified Lorentzian*

In model B, our aim is to develop the model to capture known behaviour of the wall-pressure spectrum using a modified Lorentzian spectral shape, similar to the approach of Goody (2004). We focus on the pipe-flow data from Dacome *et al.* (2025) and use scaling arguments introduced above to extend the model to the boundary-layer data from Fritsch *et al.* (2020, 2022). A key difference from (2.1) is that $g_1$ is no longer a function



https://doi.org/10.1017/jfm.2026.11550 Published online by Cambridge University Press

of $\delta^+$ as the data in Dacome *et al.* (2025) have an inner component that is fully developed. We propose that the general form of the pre-multiplied wall-pressure spectrum should be given by

$$g_i = A\,2^r \left(\frac{T_b}{T}\right)^{p_{low}} \left[1 + \left(\frac{T_b}{T}\right)^{q}\right]^{-r}, \tag{3.4}$$

which for $T_b/T \ll 1$ reduces to

$$g_i \sim A\,2^r \left(\frac{T_b}{T}\right)^{p_{low}} \Longrightarrow \phi^+_{pp} \propto f^{\,p_{low}-1}, \ \frac{\mathrm{d}\ln \phi^+_{pp}}{\mathrm{d}\ln f} \sim p_{low} - 1, \tag{3.5}$$

and $T_b$ is analogous to $\overline{T}^+$ and $\overline{T}^o$ defined in § 3.1. Note that exponents here refer to the premultiplied spectrum $f\phi^+_{pp}$; consequently, the power-law exponent of $\phi^+_{pp}$ is lower by one. Similarly, for $T_b/T \gg 1$,

$$g_i \sim A\,2^r \left(\frac{T_b}{T}\right)^{p_{low}} \left(\frac{T_b}{T}\right)^{-q\,r} \Longrightarrow \phi^+_{pp} \propto f^{\,p_{low}-q\,r-1}, \ \frac{\mathrm{d}\ln \phi^+_{pp}}{\mathrm{d}\ln f} \sim p_{low} - q\,r - 1. \tag{3.6}$$

To characterise the sharpness of the transition at $T = T_b$, define $\epsilon = T_b/T$ and $f(\epsilon) = \left[1+\epsilon^q\right]^{-r}$ so

$$\frac{\mathrm{d}\ln f}{\mathrm{d}\ln \epsilon} = -\,r\,\frac{q\,\epsilon^q}{1+\epsilon^q}, \quad \Delta(\log\epsilon) \approx \frac{2}{q}. \tag{3.7}$$

Thus $q$ directly controls the transition sharpness; larger $q$ yields a narrower region between the low- and high-frequency asymptotes.

Finally, we set

$$r = \frac{p_{low} - p_{high}}{q}, \tag{3.8}$$

so that as $T_b/T \to \infty$, the high-frequency exponent becomes $p_{high} = p_{low} - q\,r$.

3.2.1. *Inner-scale component*

The explicit form of the inner function is given with

$$g_1 = A^{in}\,2^{r^{in}} \left(\frac{T^+_{b^{in}}}{T^+}\right)^{p^{in}_{low}} \left[1 + \left(\frac{T^+_{b^{in}}}{T^+}\right)^{q^{in}}\right]^{-r^{in}}, \tag{3.9}$$

where the parameters are defined as before and $(\cdot)^{in}$ indicates the parameter associated with the inner peak. The break period $T^+_{b^{in}}$ is defined in inner units, and the amplitude $A^{in}$ is a constant that sets the magnitude of the inner peak's plateau.

Following Townsend's attached-eddy model, which predicts $\phi_{pp}(f) \sim f^0$ as $f \to 0$ for smooth-wall turbulent flows (Townsend 1976), we select

$$p^{in}_{low} = 1. \tag{3.10}$$

For the high-frequency decay, we are guided by the classical rapid-decay theories: Kraichnan (1956) suggested a steep spectrum $\phi_{pp} \sim f^{-5}$ at very high frequencies. In our formulation, a high-frequency decay of $\Phi^+_{pp,\mathrm{in}} \sim (f^+)^{-5}$ corresponds to

$$p^{in}_{high} = -6. \tag{3.11}$$



https://doi.org/10.1017/jfm.2026.11550 Published online by Cambridge University Press

| Inner function | $A^{in}$ | $T^+_{b^{in}}$ | $p^{in}_{low}$ | $p^{in}_{high}$ | $q^{in}$ | | | |
|---|---|---|---|---|---|---|---|---|
| | 1.6 | 10 | 1 | −6 | 3.5 | | | |
| Outer function | $T^{out}_b$ | $p^{out}_{low}$ | $a_A$ | $b_A$ | $a_p$ | $b_p$ | $a_q$ | $b_q$ |
| | 1.5 | 3 | 2.39 | 3.55 | −0.22 | 3.58 | −1.09 | 3.78 |

Table 2. Model B constants.

Prior studies noted that in an intermediate range around the inner peak, the wall-pressure spectrum often follows $\phi_{pp} \sim f^{-1}$ (Bradshaw 1967; Panton & Linebarger 1974; Blake 1986). To incorporate this overlap scaling, we adjust $r^{in}$ such that the slope at $f \approx f^+_{b^{in}}$ is $-1$. For a symmetric Lorentzian ($q^{in} = 2$), this condition is approximately met by $r^{in} \approx 2$. We therefore take $r^{in} = 2$ as a convenient choice that yields an overlap slope of order $-1$ (and a slightly steeper ultimate decay, closer to $f^{-6}$, at the highest frequencies). It should be noted that there is some debate in the literature regarding the exact value of the transition slope, Goody (2004), Klewicki *et al.* (2008) suggesting values closer to 0.8.

The break period $T^+_{b^{in}}$ is set based on the frequency at which the near-wall (inner) spectral contribution begins to roll off. Using experimental data for smooth-wall turbulence, we choose $f^+_{b^{in}} = 0.1$ following the observations of Morrison (2007), who identified a spectral inflection (associated with the buffer-layer peak) around that value in inner units. (This is an observation for a BL, but through the two different modelling approaches we find the break period remains consistent across pipes and BLs.)

Finally, the amplitude $A^{in}$ is tuned by matching the variance of the inner model to the variance of channel data at $\delta^+ \approx 1\,000$ (figure 6). The rationale behind this is that the inner peak is almost fully developed at this $\delta^+$ and there is only a small influence from the outer-scale energy. This yields a value of $A^{in} \approx 1.6$. A summary of the inner parameters is given in table 2.

### 3.2.2. *Outer-scale component*

We now formulate the outer-scale contribution in an analogous manner. Explicitly

$$g_2 = A^{out}\, 2^{r^{out}} \left(\frac{T^o_b}{T^o}\right)^{p^{out}_{low}} \left[1 + \left(\frac{T^o_b}{T^o}\right)^{q^{out}}\right]^{-r^{out}}, \tag{3.12}$$

where all parameters ($A^{out}$, $p^{out}_{low}$, $T^{out}_b$, $q^{out}$, $r^{out}$) pertain to the outer component.

We set $p^{out}_{low} = 3$ consistent with the notion of the outer pressure field being generated by a relatively smooth (slowly evolving) process (Cramér & Leadbetter 2013). It implies that, at the lowest frequencies, the outer pressure fluctuations are significantly attenuated ($a \sim f^2$ spectral rise from the origin, as opposed to a flat spectrum).

We associate the outer break period, $T^{out}_b$, with the characteristic turnover frequency of the largest attached eddies in the flow. This is related to the convective time scale of outer structures, of the order of $\delta/U_\delta$. We choose $T^{out}_b$ such that

$$T^{out}_b = \frac{3}{2} \tag{3.13}$$



https://doi.org/10.1017/jfm.2026.11550 Published online by Cambridge University Press

in outer units, meaning that $T_b^{out} = 3/2$ of a cycle per outer flow time, similar to the arguments presented by Jacobi *et al.* (2021). This choice is guided by prior observations of the convection speed of energetic outer-scale motions (Morrison 2007; McKeon & Sharma 2010; Jacobi *et al.* 2021), which indicate that the spectral peak associated with large-scale structures occurs at a fraction of the free-stream velocity (for BLs) or centreline velocity (for pipes).

A summary of the outer model parameters is given in table 2. The values of $A^{out}$, $p_{high}^{out}$ and $q^{out}$ are determined from the training procedure described in the next section.

### 3.2.3. *Fitted parameters for the outer component*

The outer parameters $A^{out}$, $p_{high}^{out}$ and $q^{out}$ are left free to empirically fit to the available data and aim to capture the $\delta^+$ dependent behaviour of the pressure spectra. At low $\delta^+$, outer structures are weak relative to the inner-scaled peak implying a low amplitude, steep decay and rapid roll-off. At high $\delta^+$, outer structures become stronger and populate a broader frequency range, meaning the amplitude is larger, decays more slowly and the roll-off is less steep. To incorporate this $\delta^+$ dependence, we allow $A^{out}$, $p_{high}^{out}$ and $q^{out}$ to vary with $\delta^+$. Specifically, we choose a logistic (sigmoidal) form for these dependencies, which ensures smooth transition between asymptotic values at low and high $\delta^+$

$$A^{out}(\delta^+) = \frac{1}{1 + \exp\left[a_A(b_A - \log \delta^+)\right]}, \tag{3.14a}$$

$$p_{high}^{out}(\delta^+) = -2 + \frac{1.5}{1 + \exp\left[a_p(b_p - \log \delta^+)\right]}, \tag{3.14b}$$

$$q^{out}(\delta^+) = 0.2 + \frac{0.6}{1 + \exp\left[a_q(b_q - \log \delta^+)\right]}, \tag{3.14c}$$

where $a_A, b_A, a_p, b_p, a_q, b_q$ are constants determined from data fits. The asymptotes are chosen to embed the observation that

$$\int_0^\infty g_2 \, d\log f \mapsto\approx 0 \quad \text{as} \quad \delta^+ \to 1000 \tag{3.15}$$

and to ensure stability as $\delta^+ \to \infty$.

### 3.2.4. *Fitting procedure and results*

The model is optimised on the wall-pressure spectra from Dacome *et al.* (2025) at $\delta^+ \in [4794, 47\,015]$. We note that the highest-$\delta^+$ pipe spectra require facility-specific corrections (e.g. Helmholtz resonance and background noise rejection), and such corrections are never perfect for a 1-D frequency spectrum (Appendix A). The imposed decay rates in this B form reduce concerns about overfitting to the extreme low- and high-frequency ends of the calibration spectra. However, the fitted parameters may carry some systematic uncertainty. This should be kept in mind when comparing the calibrated models with other/future measurements. The fitting procedure involves minimising the loss function, which is defined as the sum of the squared differences between the modelled and measured spectra, as well as a weighted difference between the modelled and theoretical variance proposed by Lee & Moser (2015)

$$\langle p_w^2 \rangle^+ = 2.24 \ln \delta^+ - 9.18. \tag{3.16}$$



https://doi.org/10.1017/jfm.2026.11550 Published online by Cambridge University Press

Mathematically, the loss function is defined as

$$\mathcal{L} = \sum_{\omega} \left[ f\phi_{pp}^{model} - f\phi_{pp}^{data} \right]^2 + \left[ \langle p_w^2 \rangle_{model}^{+} - \langle p_w^2 \rangle_{LM15}^{+} \right]^{0.02}. \tag{3.17}$$

The parameters are optimised using a Nelder–Mead minimisation. The optimised parameter values are reported in table 2. The variance term in (3.17) encourages consistency with the established channel-flow trend of (3.16) – although the contribution is limited by the small power coefficient – and therefore the variance scaling aims to be captured rather than independently predicted by the model.

## 4. Results

### 4.1. *Model A – log normal*

Model A comparisons with the data for BLs, pipes and channels are shown in figure 4 (left column). Best fits to the data were obtained using the constants listed in table 1. For all three flows, over the entire Reynolds-number ranges covered by the data, the model gives excellent agreement with the data. In the right column, two cases have been picked out for each flow type, separated by approximately a factor of 10 in Reynolds number. These examples illustrate how well the model reproduces the spectrum at all Reynolds numbers explored here. In addition, we see how $g_1$ and $g_2$ contribute to the total energy content, how they display significant overlap in $T^+$ over the full Reynold number range and how the inner peak evolves with Reynolds number.

The amplitudes $A_1$ for pipes and channels are Reynolds-number dependent, but only at the lower Reynolds numbers. The amplitudes $A_2$ for all three flow types depend on Reynolds number in an identical manner, with a fixed offset of 2.2, corresponding to a Reynolds number of 180. The values of $\overline{T}^+$ and $\overline{T}^o$ are more or less as expected from our earlier discussion, with the exception of $\overline{T}^o$ for pipes, which is considerably smaller than the values for BLs and channels. This suggests a comparatively slower growth of the low-frequency contribution in pipes – a point not emphasised in prior work.

### 4.2. *Model B – modified Lorentzian*

With similar success, model B matches well with the inner and outer components summed to reconstruct the original wall-pressure spectrum given by (2.1). The expanded view in figure 5 shows the modelled vs measured wall-pressure spectra at the range of Reynolds numbers measured in Dacome *et al.* (2025). By design, the inner-scaled contribution remains invariant with $\delta^+$, and the outer-scaled contribution varies with $\delta^+$. In figure 5(*h*), we show an illustrative extrapolation of model B to $\delta^+ = 5 \times 10^5$ to demonstrate the internal consistency of the continuous asymptotic formulation. This extrapolation does not constitute independent validation and should be interpreted cautiously given the finite calibration range and the experimental uncertainties at the spectral extremes (Appendix A). The inner peak in the predicted spectrum has moved outside the range of human hearing here and the outer peak centres around 2000 Hz and contains the majority of the energy.

Model B was primarily developed for turbulent pipe flow, but it can be extended to boundary-layer flows by adjusting some chosen parameters. Namely, we change the outer break period to $T_b^{out} = 3.45$, consistent with the longer outer-scaled structures observed by Lee & Sung (2013) in boundary-layer flows. The amplitude $A^{out}$ is also increased by a factor of 1.56 to account for the different scaling of the wall-pressure spectrum in BLs. The inner component remains unchanged, as the near-wall pressure fluctuations are expected



https://doi.org/10.1017/jfm.2026.11550 Published online by Cambridge University Press

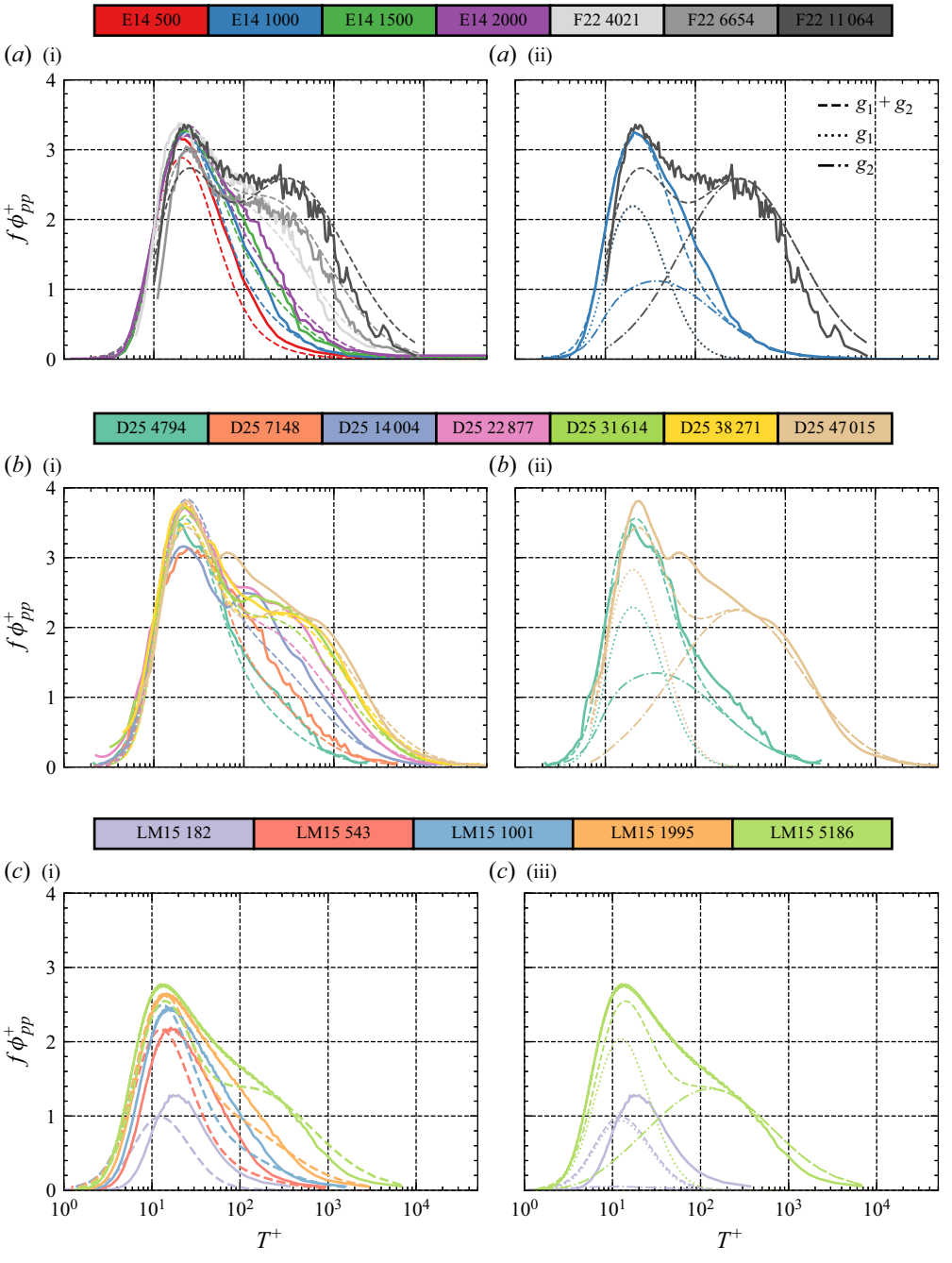



Figure 4. Comparison of model A with data shown in figure 1. Model constants listed in table 1. (*a*) BLs. Left: all $\delta^+$. Right: $\delta^+ = 1000$, 11 064, showing $g_1$ and $g_2$ ($g_1$ is identical for these $\delta^+$). (*b*) Pipes. Left: all $\delta^+$. Right: $\delta^+ = 4794$, 47 015, showing $g_1$ and $g_2$. (*c*) Channels. Left: all $\delta^+$. Right: $\delta^+ = 550$, 5200 showing $g_1$ and $g_2$.

https://doi.org/10.1017/jfm.2026.11550 Published online by Cambridge University Press

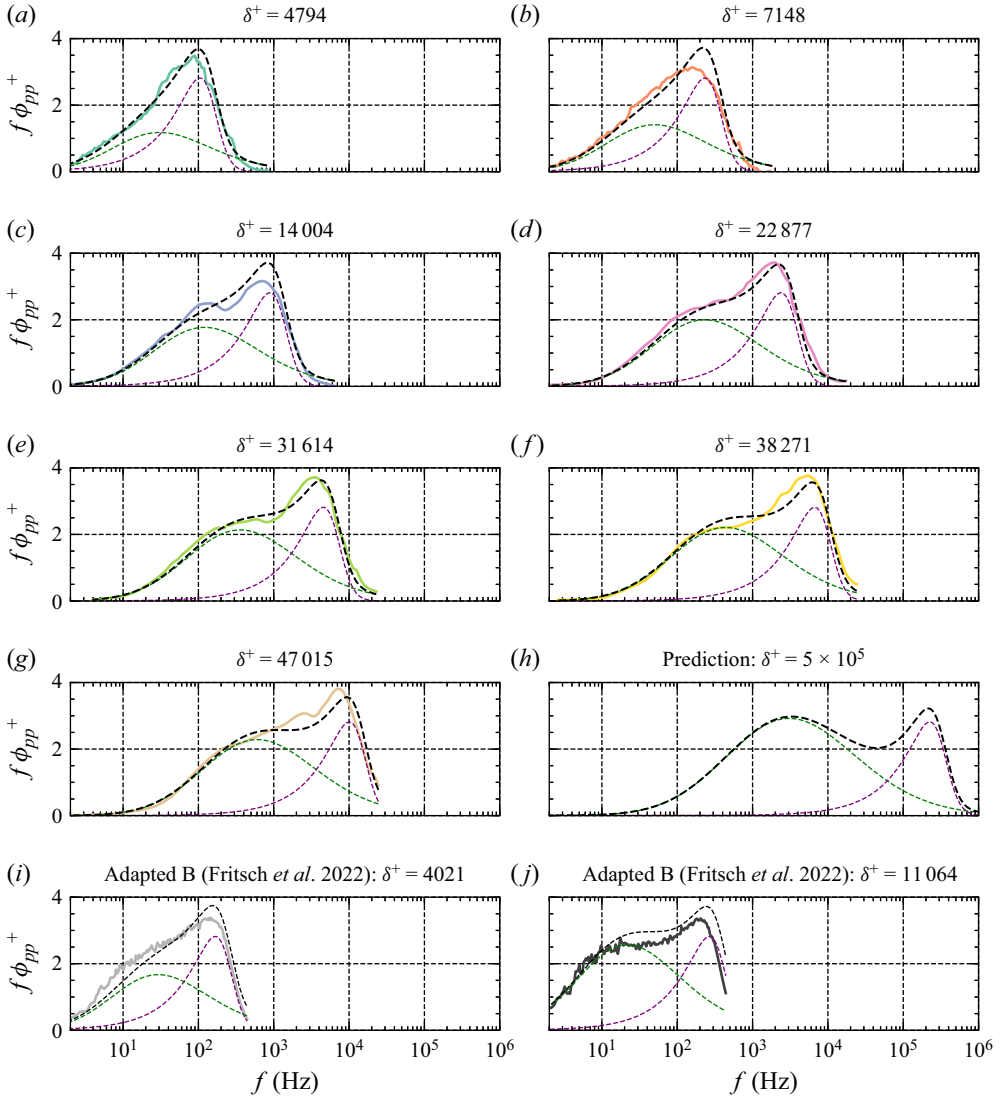



Figure 5. The modelled vs measured wall-pressure spectra at the range of Reynolds numbers measured in Dacome *et al.* (2025) (*a–g*). The solid lines are the measured spectra, the dashed lines are the modelled spectra. The purple dashed line is $g_1$ for model B, and the green dashed line is $g_2$. In panel (*h*), illustrative extrapolation of the spectrum at $\delta^+ = 5 \times 10^5$. Panels (*i,j*) correspond to the data and the adapted model B predictions at the labelled $\delta^+$ values.

to be similar in both pipe and boundary-layer flows. The resulting model for boundary-layer flows is tested against Fritsch *et al.* (2022). Although this is not a true prediction, as the coefficients are tuned using observed trends, good agreement is obtained for both the low-$\delta^+ = 4021$ and high-$\delta^+ = 11\,064$ cases.

### 4.3. *Variance*

Turbulent wall-pressure fluctuations are known to intensify with increasing Reynolds number. Both experimental and numerical studies have observed that the wall-pressure variance, $\langle p_w'^2 \rangle^+ = \langle p_w'^2 \rangle / \tau_w^2$, grows approximately logarithmically with the friction



https://doi.org/10.1017/jfm.2026.11550 Published online by Cambridge University Press

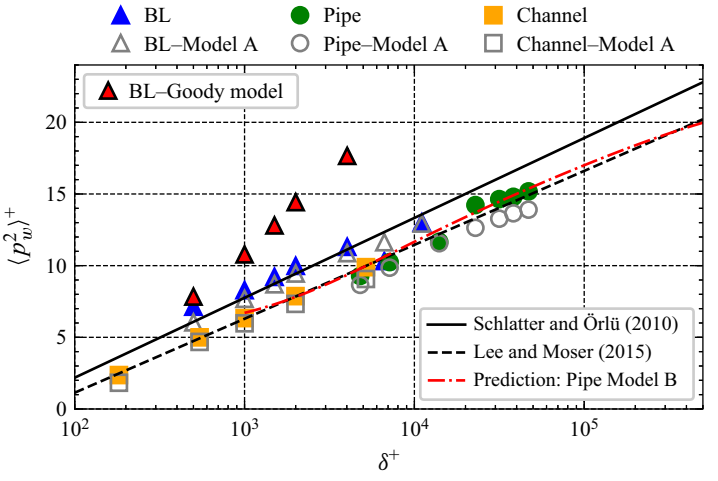



Figure 6. Variance of wall-pressure fluctuations. The solid markers are the data described in figure 1, where: ▲ is the boundary-layer data, ● the pipe and ■ the channel. The Goody-model variance is ▲. Model A is shown with grey open symbols matching the data. Model B over $\log \delta^+ \in [3, 5]$ is denoted by $-\cdot$. For comparison, the empirical relations are $-$ for the boundary-layer correlation $\langle p_w'^2 \rangle^+ = 2.42 \ln \delta^+ - 8.96$ of Schlatter & Örlü (2010) and $--$ for the channel correlation $\langle p_w'^2 \rangle^+ = 2.24 \ln \delta^+ - 9.18$ Lee & Moser (2015).

Reynolds number, $\delta^+$ (Farabee & Casarella 1991; Panton *et al.* 2017). This behaviour is consistent with Townsend's (1951) attached-eddy hypothesis, Townsend (1951) which postulates that as $\delta^+$ increases a broader range of self-similar eddies contributes to the pressure field, producing a $k_x^{-1}$ spectral region whose integration leads to the scaling $\langle p_w'^2 \rangle^+ \propto \ln(\delta^+)$. For instance, the boundary-layer experiments of Farabee & Casarella (1991), in the range $\delta^+ \approx 10^3$–$2 \times 10^3$, clearly demonstrated a rise in $\langle p_w'^2 \rangle^+$ with Reynolds number, which they attributed to an expanding $f^{-1}$ range in the pressure spectrum. Despite the evident growth of the low-frequency range with Reynolds number, and the consequent departure from $f^{-1}$ scaling, the logarithmic dependence appears to be quite robust, even at very high Reynolds numbers (Klewicki *et al.* 2008; Panton *et al.* 2017).

The variance $\langle p_w'^2 \rangle^+$ is found by integrating the spectra over all frequencies. The results for both models and the underlying data are shown in figure 6. As expected from the good agreement between the model spectra and the data, the variances calculated for the model and data agree very well. Furthermore, the boundary-layer results for model A agree well with the correlation proposed for BLs by Schlatter & Örlü (2010) ($\langle p_w'^2 \rangle^+ = 2.42 \ln \delta^+ - 8.96$), and the pipe and channel results agree well with the correlation proposed for channels by Lee & Moser (2015) (3.16), with the continuous form of model B also aligning with (3.16) by design (cf. (3.17)) and extending in its continuous predictive form to $\delta^+ = 5 \times 10^5$. The similarity across the channel and pipe variance matches well with the findings of Yu, Ceci & Pirozzoli (2022), Wei & Pirozzoli (2025). The Goody model shows a major disagreement with these other trends, significantly overpredicting the variance.

We can also relate the wall-pressure variance to the wall-shear stress variance by combining the correlation obtained by Samie *et al.* (2018) for $\langle u_p'^2 \rangle^+$, the maximum value of the inner peak in the streamwise Reynolds stress

$$\langle u_p'^2 \rangle^+ = \frac{\langle u_p'^2 \rangle}{u_\tau^2} = 3.54 + 0.646 \ln \delta^+, \tag{4.1}$$



https://doi.org/10.1017/jfm.2026.11550 Published online by Cambridge University Press

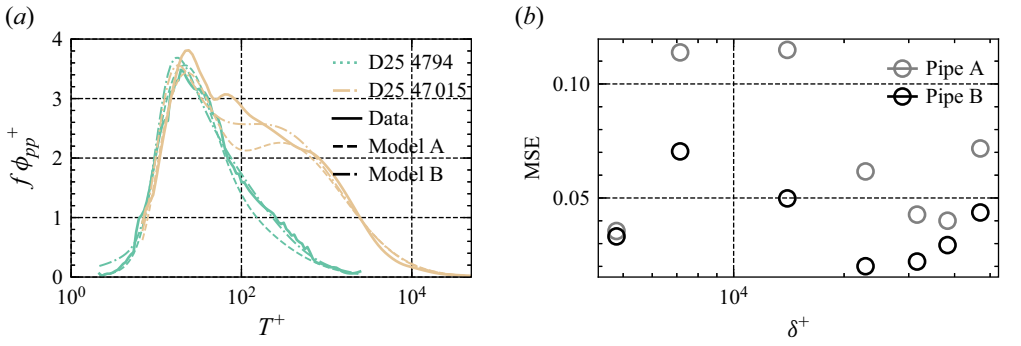



Figure 7. Comparing model A and model B with pipe-flow data. (*a*) Data from Dacome *et al.* (2025) at $\delta^+ = 4794$ to 47 015. (*b*) Mean squared error (MSE) for model A and model B.

with

$$\langle u_p'^2 \rangle^+ \approx 46 \langle \tau_w'^2 \rangle^+ \tag{4.2}$$

(Smits *et al.* 2021; Chen & Sreenivasan 2021). Then, by using the correlation for $\langle u_p'^2 \rangle^+$ proposed by Schlatter & Örlü (2010)

$$\frac{\langle p_w'^2 \rangle^+}{\langle u_p'^2 \rangle^+} \approx \frac{\langle p_w'^2 \rangle^+}{46 \langle \tau_w'^2 \rangle^+} = \frac{2.42 \ \ln \delta^+ - 8.96}{3.54 + 0.646 \ \ln \delta^+}, \tag{4.3}$$

we obtain a tentative connection between the variances in wall pressure and wall-shear stress – in addition to connecting both with the magnitude of the inner peak in $\overline{u^2}$. This suggests a previously unreported correlation between wall-pressure and wall-shear stress variances based on reported correlations using the same variables. This construction is heuristic and should not be interpreted as a derivation from the governing equations or as an established causal connection; its validity and universality (including the assumed linkage between the inner peak and wall-shear behaviour) remain an active topic of discussion in the literature (e.g. Marusic, Baars & Hutchins 2017). Direct, simultaneous measurements of wall-pressure and wall-shear-stress fluctuations at high Reynolds number would be required to assess whether such a relationship holds quantitatively.

## 5. Discussion and consequences

We have shown that it is possible to model the energy content of the wall-pressure signal using two functions: an inner-scaled function $g_1$ and an outer-scaled function $g_2$. Both models proposed here reproduce the pre-multiplied spectra and the variances for BLs and pipes, with model A extending down to the channel-flow data.

Models A and B are compared in figure 7 for pipe flow at two Reynolds numbers, $\delta^+ = 4794$ and $\delta^+ = 47\,015$. The left panel shows the spectra along with the modelled forms, and the right panel shows the mean squared error (MSE) between the two models across the frequency range. The MSE is calculated as



https://doi.org/10.1017/jfm.2026.11550 Published online by Cambridge University Press

$$\mathrm{MSE_A} = \frac{1}{N}\sum_{i=1}^{N}\left(\phi_{pp}^{Model\,A}(f_i) - f\phi_{pp}(f_i)^{+}\right)^2, \tag{5.1a}$$

$$\mathrm{MSE_B} = \frac{1}{N}\sum_{i=1}^{N}\left(\phi_{pp}^{Model\,B}(f_i) - f\phi_{pp}(f_i)^{+}\right)^2, \tag{5.1b}$$

where $N$ is the number of frequency points and $f_i$ are the discrete frequency values. Both models show a good agreement with the data, with model B generally performing better despite the extra asymptotic constraints. The close agreement between the models is a feature as we believe they serve a complementary purpose: model A for compact reproduction with minimal inputs; model B when one wishes to enforce asymptotic exponents and smooth $\delta^+$-dependence (3.14*a*–*c*).

For both models, the function $g_1$ models the inner-scaled peak, and it has a characteristic time constant $\overline{T}^+ = 12$–$20$ (see tables 1 and 2). The convection velocity for this inner-scaled peak is often taken to be $U_c^+ = 10$–$12$ (Ghaemi, Ragni & Scarano 2012; Dacome *et al.* 2025), which corresponds approximately to the mean velocity at the location of the inner peak in the streamwise Reynolds stress $\overline{u_p^2}^+$ (located at $y^+ \approx 15$). As mentioned (cf. § 1), the convection velocity is wavenumber-dependent, our use of constant values helps to give insight without being prescriptive. This time constant $\overline{T}^+$ is an order of magnitude smaller than the average period of the near-wall bursting events, which is approximately 100 (Metzger, McKeon & Arce-Larreta 2010). The corresponding wavelength $\lambda_{x1} = U_c\overline{T_1}$, so that $\lambda_{x1}^+ = 10\overline{T}^+ = O(100)$, and it matches the characteristic spacing between the near-wall streaks (Smith & Metzler 1983). The lower $T^+$ of the inner peak observed in channel flow compared with pipe and boundary-layer flows likely arises from the length-scale dependence of the convection velocity. The channel DNS data of Lee & Moser (2015) are converted to frequency space using a fixed $U_c^+ = 10$; however, Del Álamo & Jiménez (2009) and Damani *et al.* (2025) show that high-$k_x$, short-$T$ motions, and subsequent pressure fluctuations, convect more slowly, which would artificially shift the inner peak to lower $T^+$. For reference, the peak in the time-resolved spectra of Anantharamu & Mahesh (2020) occurs at $T^+ \approx 18$, consistent with the pipe and boundary-layer data.

As a complement to $g_1$, the function $g_2$ models the outer-scaled peak, with a characteristic time constant $\overline{T}^o = 0.2$–$0.8$ (see table 1). The convection velocity connected with this outer-scaled peak is $U_c = 0.7U_e$ (Damani *et al.* 2024*b*) (many other values have been proposed, ranging from $0.6U_e$ (Chase & Noiseux 1982) to $0.819U_e$ (Hu, Morfey & Sandham 2002)) which corresponds to the mean velocity at a location near the outer part of the logarithmic region. The matching wavelength $\lambda_{x2}^o = U_c/U_e\overline{T^o}$, so that the streamwise wavelength $\lambda_{x2}^o = 0.7\overline{T}^o \approx 0.14$–$0.56$, and the matching wavenumber is $k_x^o \approx 11$–$45$. The evidence, therefore, suggests that the outer-scaled peak is associated with motions typical of the inertial layer; these are considerably smaller than the size of the large-scale motion and very-large-scale motion. It would be of interest to relate $g_2$ more explicitly to the attached-eddy picture, but this would require a more detailed study to disentangle the wall-pressure imprint of different eddy populations in the projected spectrum.

In this paper, we have focused on canonical flow cases, demonstrating that our simple models can give an accurate representation of the wall-pressure spectrum over a wide range of Reynolds numbers. However, the models are not expected to be valid for flows with significant pressure gradients, compressibility effects or roughness, as these



https://doi.org/10.1017/jfm.2026.11550 Published online by Cambridge University Press

conditions can significantly alter the scaling of the wall-pressure spectrum. Nevertheless, following on from the approach taken by Gustenyov *et al.* (2025), we believe that our simple modelling approach can be extended to incorporate these variations in flow physics by adjusting the components accordingly. For example, we might model roughness by changing $g_1$ and pressure gradient by altering $g_2$. In this way, we hope to learn more about the physical underpinning the influence of our two basic spectral components on the wall-pressure spectrum.

The model faithfully reproduces the temporal wall-pressure spectra and – as Damani *et al.* (2025) demonstrate – the spatial relationship is required to complete the picture. Ongoing work looks at understanding the physical mechanisms responsible for the logarithmic growth of $\phi_{pp}$ as part of the Shear stress and Propagating Pressure measurements in High Reynolds number Experiments (SAPPHiRE) campaign.

**Acknowledgements.** We would like to thank the authors of the original datasets for making their data openly available, and for their efforts in collecting high-quality data at high Reynolds numbers. We also thank Dr T. Jaroslawski, Professor I. Marusic, Dr V. Gudla for their helpful comments in the development of this work.

**Funding.** The partial support of DARPA under award no. HR0011-24-9-0465 is gratefully acknowledged.

**Declaration of interests.** The authors report no conflicts of interest.

**Data availability statement.** The data that support the findings of this study are openly available in repositories associated with Fritsch *et al.* (2020, 2022) and Lee & Moser (2015). The pipe-flow data were reconstructed from Dacome *et al.* (2025). Upon request, we are happy to share the model code used to generate the results in this paper.

## Appendix A. Observations on the data

There are three possible issues surrounding the quality and completeness of the data used in the modelling. First, the highest-Reynolds-number boundary-layer profile ($\delta^+ = 11\,064$) was obtained downstream of a mild pressure-gradient history imposed on the tunnel wall by the presence of an airfoil in the free stream (Fritsch *et al.* 2020, 2022). In figure 8(*a*), we show the pressure coefficient distributions measured when the airfoil was placed at angles of attack $\alpha = 0°$, –4° and –10°. Figure 8(*b*) demonstrates that the presence of the airfoil has little effect on the wall-pressure spectrum at the most upstream station ($x = 1.95$ m), even at $\alpha = -10°$. Figure 8(*c*) similarly demonstrates that for $\alpha < 4°$ the presence of the airfoil has little effect on the wall-pressure spectrum at the most downstream station ($x = 4.91$ m) where the $\delta^+ = 11\,064$ profile was measured. We propose, therefore, that all the experimental data on BLs shown in figure 1 are free of any significant effects of pressure gradient.

Second, the boundary-layer LES and channel-flow DNS were obtained in a limited domain which may affect the resolution of the largest outer-scale motions. For the boundary-layer data, the computation is for a spatially evolving flow, and so the principal limitation on resolving the wall-pressure spectrum is the maximum averaging time. Although Eitel-Amor *et al.* (2014) do not specify the sampling time, the earlier work by Schlatter & Örlü (2010) indicate values of 50 000 viscous time units, or 36 outer time units at $Re_\theta = 4300$ ($\delta^+ = 1370$). From figure 1, we see that this appears to be sufficient to resolve the complete spectrum for each Reynolds number. For the channel-flow data, the domain size could be a limitation, but for this computation it was $8\pi\delta$, corresponding to $T^+ = 660$ at $\delta^+ = 550$ and $T^+ = 4900$ at $\delta^+ = 5200$. From figure 1, we see that this appears to be sufficient to resolve the complete spectrum for each Reynolds number.



https://doi.org/10.1017/jfm.2026.11550 Published online by Cambridge University Press

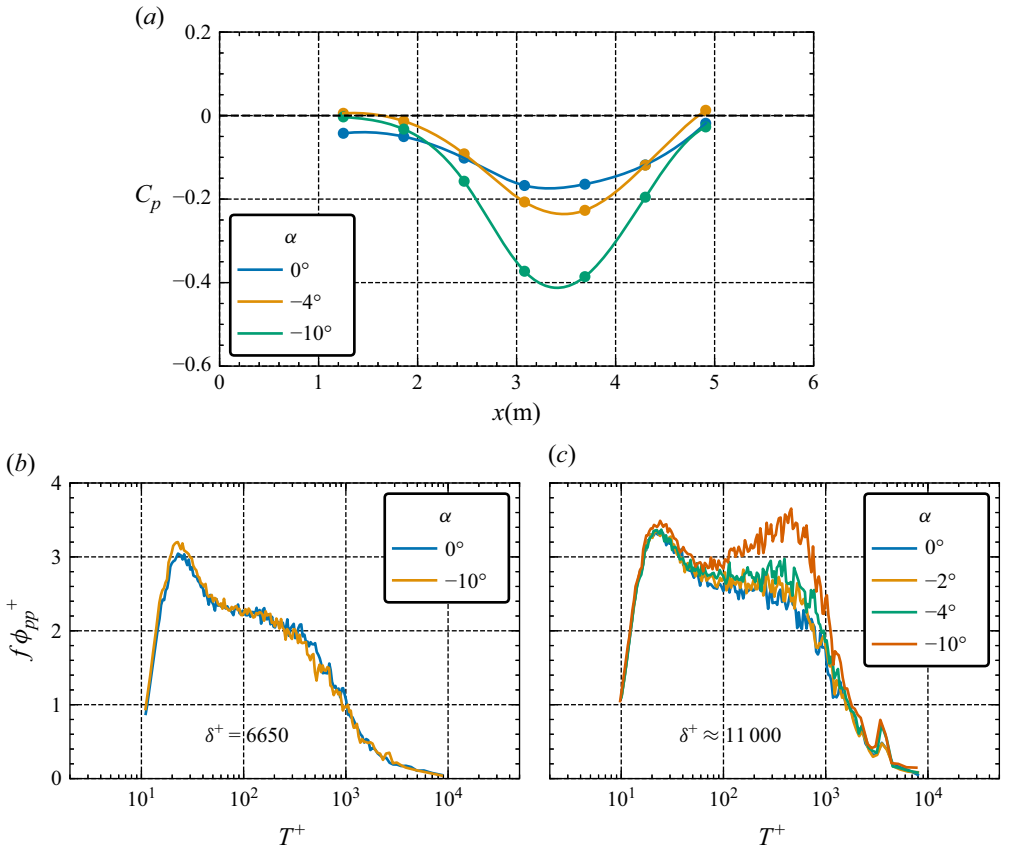



Figure 8. Data from University of Virginia experiments on the tunnel wall for different airfoil angles of attack ($\alpha$) at 58 m s$^{-1}$ (Fritsch *et al.* 2020, 2022). (*a*) Pressure coefficient distributions. (*b*) Pre-multiplied spectra of wall-pressure fluctuations at $x = 1.25$ m ($\delta^+ = 6650$). (*c*) Pre-multiplied spectra of wall-pressure fluctuations at $x = 4.91$ m ($\delta^+ \approx 11000$).

Third, experimental data taken with a pinhole cap for the microphone suffer from Helmholtz resonance depending on the cavity between the microphone membrane and the cap. A common correction used is to fit an empirical model to calibration data and correct the resulting spectra with a transfer function. The model is not a perfect representation of the individual pinhole and perfect correction is nearly impossible. The result is an error in the spectra where the true cap effects are not perfectly accounted for.

Fourth, considerations should be made when comparing experimental datasets due to the background noise rejection which is different in each facility. Background noise removal from coherent pressure fluctuations that are not a result of the boundary-layer physics can be done through various methods. The techniques of background noise removal can lead to discrepancies between experimental facilities in the low-frequency region.

Fifth, the experimental data are limited by the frequency response of the wall-pressure sensor. Figure 9(*a*) shows pre-multiplied spectra of wall-pressure fluctuations for the boundary-layer data, with horizontal bars show range of $T^+$ corresponding to the frequency response of the pressure measurements (20 Hz to 16 kHz). Figure 9(*b*) shows the corresponding limits for the pipe-flow data (10 Hz to 40 kHz). The boundary-layer data at high $T^+$ (low frequencies) are well resolved at all three Reynolds numbers,



https://doi.org/10.1017/jfm.2026.11550 Published online by Cambridge University Press

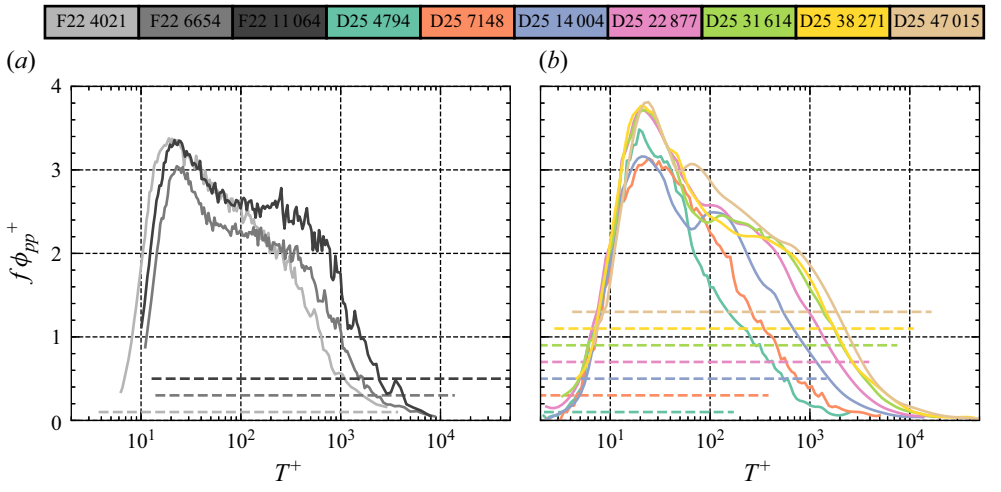



Figure 9. Pre-multiplied spectra of wall-pressure fluctuations. Wall-pressure sensor frequency response given by horizontal bars, colour corresponding to spectral data. (*a*) BLs for $\delta^+ = 4021$ to 11064 (Fritsch *et al.* 2020, 2022). (*b*) Pipe flows for $\delta^+ = 4794$ to 47 015 (Dacome *et al.* 2025).

but the data for $\delta^+ = 6654$ and 11 064 appear to be significantly filtered at low $T^+$ (high frequencies). The pipe-flow data are affected somewhat in reverse, in that the low $T^+$ data are well resolved, but the high $T^+$ data are significantly filtered at the lowest three Reynolds numbers. Despite the limitation on the frequency response, the effects of the filtering are relatively minor in terms of model presented here.

Sixth, the $u_\tau^4$ dependence of the pre-multiplied spectra and the $u_\tau^2$ dependence on $T^+$ puts a great burden on measurements of $u_\tau$. The amplification in error affects both the height and $T^+$ position of the peak.

## References


Anantharamu, S. & Mahesh, K. 2020 Analysis of wall-pressure fluctuation sources from direct numerical simulation of turbulent channel flow. *J. Fluid Mech.* **898**, A17.

Baars, W.J. & Marusic, I. 2020 Data-driven decomposition of the streamwise turbulence kinetic energy in boundary layers. Part 1. Energy spectra. *J. Fluid Mech.* **882**, A25.

Blake, W.K. 1986 *Mechanics of Flow-Induced Sound and Vibration V1: General Concepts and Elementary Sources*, vol. 1. Elsevier.

Bradshaw, P. 1967 Inactive' motion and pressure fluctuations in turbulent boundary layers. *J. Fluid Mech.* **30** (2), 241–258.

Chase, D.M. & Noiseux, C.F. 1982 Turbulent wall pressure at low wavenumbers: relation to nonlinear sources in planar and cylindrical flow. *J. Acoust. Soc. Am.* **72** (3), 975–982.

Chen, X. & Sreenivasan, K.R. 2021 Reynolds number scaling of the peak turbulence intensity in wall flows. *J. Fluid Mech.* **908**, R3.

Corcos, G.M. 1964 The structure of the turbulent pressure field in boundary-layer flows. *J. Fluid Mech.* **18** (03), 353.

Cramér, H. & Leadbetter, M.R. 2013 *Stationary and Related Stochastic Processes: Sample Function Properties and Their Applications*. OCLC: 1162479530.

Dacome, G., Lazzarini, L., Talamelli, A., Bellani, G. & Baars, W.J. 2025 Scaling of wall-pressure–velocity correlations in high-Reynolds-number turbulent pipe flow. *J. Fluid Mech.* **1013**, A48.

Damani, S., Butt, H., Devenport, W.J. & Lowe, T. 2024*a* Evaluating models for sub-convective pressure fluctuations in turbulent boundary layers. In *30th AIAA/CEAS Aeroacoustics Conference*.

Damani, S., Butt, H., Totten, E., Chaware, S., Sharma, B., Devenport, W.J. & Lowe, T. 2024*b* The characteristics of sub-convective wall pressure fluctuations in a turbulent boundary layer. In *AIAA SCITECH 2024 Forum*.




https://doi.org/10.1017/jfm.2026.11550 Published online by Cambridge University Press

DAMANI, S., BUTT, H., TOTTEN, E., DEVENPORT, W.J. & LOWE, T. 2025 Measurement and analysis of sub-convective wall pressure fluctuations in turbulent boundary layer flows. *J. Fluid Mech.* **1014**, A26.
DEL ÁLAMO, J. C. & J., JIMÉNEZ 2009 Estimation of turbulent convection velocities and corrections to Taylor's approximation. *J. Fluid Mech.* **640**, 5–26.
EITEL-AMOR, G., ÖRLÜ, R. & SCHLATTER, P. 2014 Simulation and validation of a spatially evolving turbulent boundary layer up to. *Intl J. Heat Fluid Flow* **47**, 57–69.
FARABEE, T.M. & CASARELLA, M.J. 1991 Spectral features of wall pressure fluctuations beneath turbulent boundary layers. *Phys. Fluids A* **3** (10), 2410–2420.
FRITSCH, D., VISHWANATHAN, V., DUETSCH-PATEL, J., GARGIULO, A., LOWE, K.T. & DEVENPORT, W.J. 2020 The pressure signature of high Reynolds number smooth wall turbulent boundary layers in pressure gradient family. In *AIAA AVIATION 2020 FORUM*.
FRITSCH, D.J., VISHWANATHAN, V., TODD LOWE, K. & DEVENPORT, W.J. 2022 Fluctuating pressure beneath smooth wall boundary layers in nonequilibrium pressure gradients. *AIAA J.* **60** (8), 4725–4743.
GHAEMI, S., RAGNI, D. & SCARANO, F. 2012 PIV-based pressure fluctuations in the turbulent boundary layer. *Exp. Fluids* **53**, 1823–1840.
GIBEAU, B. & GHAEMI, S. 2021 Low- and mid-frequency wall-pressure sources in a turbulent boundary layer. *J. Fluid Mech.* **918**, A18.
GOODY, M. 2004 Empirical spectral model of surface pressure fluctuations. *AIAA J.* **42** (9), 1788–1794.
GUSTENYOV, N., BAILEY, S.C.C. & SMITS, A.J. 2025 A model spectrum for turbulent wall-bounded flow. *J. Fluid Mech.* **1016**, A23.
HASAN, A.M., COSTA, P., LARSSON, J. & PECNIK, R. 2025 Scaling of wall pressure and the peak of streamwise turbulence intensity in compressible wall flows. arXiv: 2505.07407.
HU, Z.W., MORFEY, C.L. & SANDHAM, N.D. 2002 Aeroacoustics of wall-bounded turbulent flows. *AIAA J.* **40** (3), 465–473.
HU, Z.W., MORFEY, C.L. & SANDHAM, N.D. 2006 Wall pressure and shear stress spectra from direct simulations of channel flow. *AIAA J.* **44** (7), 1541–1549.
HWANG, Y.F., BONNESS, W.K. & HAMBRIC, S.A. 2009 Comparison of semi-empirical models for turbulent boundary layer wall pressure spectra. *J. Sound Vib.* **319** (1–2), 199–217.
JACOBI, I., CHUNG, D., DUVVURI, S. & MCKEON, B.J. 2021 Interactions between scales in wall turbulence: phase relationships, amplitude modulation and the importance of critical layers. *J. Fluid Mech.* **914**, A7.
KLEWICKI, J.C., PRIYADARSHANA, P.J.A. & METZGER, M.M. 2008 Statistical structure of the fluctuating wall pressure and its in-plane gradients at high Reynolds number. *J. Fluid Mech.* **609**, 195–220.
KRAICHNAN, R.H. 1956 Pressure fluctuations in turbulent flow over a flat plate. *J. Acoust. Soc. Am.* **28** (3), 378–390.
LEE, J.H. & SUNG, H.J. 2013 Comparison of very-large-scale motions of turbulent pipe and boundary layer simulations. *Phys. Fluids* **25** (4), 045103.
LEE, M. & MOSER, R.D. 2015 Direct numerical simulation of turbulent channel flow up to. *J. Fluid Mech.* **774**, 395–415.
MARUSIC, I., BAARS, W.J. & HUTCHINS, N. 2017 Scaling of the streamwise turbulence intensity in the context of inner-outer interactions in wall turbulence. *Phys. Rev. Fluids* **2** (10), 100502.
MCKEON, B.J. & SHARMA, A.S. 2010 A critical-layer framework for turbulent pipe flow. *J. Fluid Mech.* **658**, 336–382.
METZGER, M.M., MCKEON, B.J. & ARCE-LARRETA, E. 2010 Scaling the characteristic time of the bursting process in the turbulent boundary layer. *Phys. D: Nonlinear Phenom.* **239** (14), 1296–1304.
MORRISON, J.F. 2007 The interaction between inner and outer regions of turbulent wall-bounded flow. *Phil. Trans. R. Soc. A.* **365** (1852), 683–698.
PANTON, R.L., LEE, M. & MOSER, R.D. 2017 Correlation of pressure fluctuations in turbulent wall layers. *Phys. Rev. Fluids* **2** (9), 094604.
PANTON, R.L. & LINEBARGER, J.H. 1974 Wall pressure spectra calculations for equilibrium boundary layers. *J. Fluid Mech.* **65** (2), 261–287.
PIROZZOLI, S. & WEI, T. 2025 On pressure fluctuations in the near-wall region of turbulent flows. *J. Fluid Mech.* **1010**, A10.
SAMIE, M., MARUSIC, I., HUTCHINS, N., FU, M.K., FAN, Y., HULTMARK, M. & SMITS, A.J. 2018 Fully resolved measurements of turbulent boundary layer flows up to. *J. Fluid Mech.* **851**, 391–415.
SCHLATTER, P. & ÖRLÜ, R. 2010 Assessment of direct numerical simulation data of turbulent boundary layers. *J. Fluid Mech.* **659**, 116–126.
SMITH, C.R. & METZLER, S.P. 1983 The characteristics of low-speed streaks in the near-wall region of a turbulent boundary layer. *J. Fluid Mech.* **129**, 27–54.



https://doi.org/10.1017/jfm.2026.11550 Published online by Cambridge University Press

SMITS, A.J., HULTMARK, M., LEE, M., PIROZZOLI, S. & WU, X. 2021 Reynolds stress scaling in the near-wall region of wall-bounded flows. *J. Fluid Mech.* **926**, A31.

SMITS, A.J., MCKEON, B.J. & MARUSIC, I. 2011 High-reynolds number wall turbulence. *Annu. Rev. Fluid Mech.* **43** (1), 353–375.

SMOL'YAKOV, A.V. 2006 A new model for the cross spectrum and wavenumber-frequency spectrum of turbulent pressure fluctuations in a boundary layer. *Acoust. Phys+.* **52** (3), 331–337.

TAYLOR, G.I. 1938 The spectrum of turbulence. *Proc. R. Soc. Lond. A Math. Phys. Sci.* **164** (919), 476–490.

TOWNSEND, A.A. 1951 The structure of the turbulent boundary layer. *Math. Proc. Camb. Phil. Soc.* **47** (2), 375–395.

TOWNSEND, A.A. 1976 The structure of turbulent shear flow. *Z. Angew. Math. Mech.* **56** (9), 448–448.

WEI, T., FIFE, P., KLEWICKI, J. & MCMURTRY, P. 2005 Properties of the mean momentum balance in turbulent boundary layer, pipe and channel flows. *J. Fluid Mech.* **522**, 303–327.

WEI, T. & PIROZZOLI, S. 2025 Scaling of pressure fluctuation in turbulent internal flows. *J. Fluid Mech.* **1010**, A54.

YU, M., CECI, A. & PIROZZOLI, S. 2022 Reynolds number effects and outer similarity of pressure fluctuations in turbulent pipe flow. *Int. J. Heat Fluid Flow* **96**, 108998.

ZHAO, K., LI, Y., PEI, R., LI, H. & BENNETT, G.J. 2025 Review of wavenumber-frequency spectrum models of turbulent boundary-layer wall pressure fluctuations. *AIAA J.* **63** (3), 1140–1166.

https://doi.org/10.1017/jfm.2026.11550 Published online by Cambridge University Press